Simulating Whole-Body PET Scanning with Rapid Analytical Methods [1]

C. Comtat[1], *Member, IEEE*, P.E. Kinahan[1], *Member, IEEE*, M. Defrise[2], C. Michel[3], *Member, IEEE*, C. Lartizien[4], D.W. Townsend[1] *Senior Member, IEEE*

[1]Department of Radiology, University of Pittsburgh, Pittsburgh, U.S.A.

[2]Division of Nuclear Medicine, Free University of Brussels AZ-VUB, Brussels, Belgium

[3]PET Laboratory, Catholic University of Louvain, Louvain La Neuve, Belgium

[4]Frederic Joliot Hospital, Department of Medical Research, CEA, Orsay, France

Abstract

We present a 3D whole-body PET simulator that generates multiple, yet statistically accurate, realizations of projection data within a computation time that is short enough to enable the measurement of the task performance of image reconstruction algorithms. The whole-body simulator takes into account the following effects: the seperate amounts of statistical noise contributed by true, scattered, and random coincidences, activity outside the field of view, activity decay between bed positions, detector efficiencies and resolution, and noise arising from the transmission scan. The principle of the simulation is to analytically calculate projections based on the geometrical specification of the emission and attenuation objects that comprise the MCAT phantom. A pre-determined level of statistical noise is then added to the projection data, which is then inputted to the same data correction and image reconstruction procedures used in practice.

We compare the results of multiple realizations of simulated and measured phantom studies at statistical noise levels similar to those encountered in 3D whole-body PET scanning. We obtain comparable statistical noise properties for the fully corrected emission sinograms, and also show that a simple model accurately predicts the statistical noise added by random and scattered coincidences generated by activity outside the field of view.

I. Introduction

In order to properly test the task performance of different PET reconstruction algorithms with simulated data, it is important that the generated data have realistic statistical properties. This is a critical issue for whole-body scanning, where image quality is often limited by stochastic noise.

Furuie et al. [1] used a non Monte Carlo technique to generate statistically accurate realizations of the projection data for 3D brain PET imaging. Monte Carlo methods are potentially more accurate, but are currently too computationally intensive to allow generating the multiple independent realizations needed for estimating the true variance of the generated sinograms or reconstructed images. We used a similar approach to that of Furuie et al. to develop a simulator for 3D whole-body PET that additionally incorporates the following effects: the seperate amounts of statistical noise contributed by true, scattered, and random coincidences, activity outside the field of view, activity decay between bed positions, detector efficiencies and resolution, and noise arising from the transmission scan.

The principle of the simulation is to first analytically calculate projections based on the geometrical specification of the emission and attenuation objects. This avoids potential non-physical interactions with numerically integrated system matrices used in iterative methods. A pre-determined level of statistical noise is then added to the projection data, which are then inputted to the same data correction and image reconstruction procedures used in practice. As the projections are not numerically integrated, this simulation is well-suited to compare different statistical reconstruction methods [2] but is not intended to test the accuracy of correction procedures like the scattered coincidences detection. Our goal is not to accurately simulate the detection of random and scattered coincidences, but rather to simulate their effect on the noise of the emission and transmission scan. We present here a description of our simulator and a comparison between simulated projections and measured phantom data that were acquired under noise conditions typical of whole-body scanning.

II. Simulator Description

A. Noise model

In PET imaging, Poisson noise is contributed from four sinograms: the emission, transmission, normalization, and blank scans. We assume that no significant noise is contributed by the normalization and blank scans as they can be acquired for a long duration. For each scan there are potentially three types of detected events: true, random, and scattered coincidences. We assume that the fraction of scattered coincidences in the transmission scan is not significant (such as in a rod-windowed scan) and that there is no contamination from the emission objects to the transmission sinogram. We are left with five independent Poisson noise sources: t_{E}, r_{E}, s_{E}, t_{T}, and r_{T} , where t stands for true coincidences, r for random coincidences, and s for scattered coincidences. The subscripts E and T refer to coincident events in the emission or transmission scan. The sinogram elements t_{E}, r_{E}, s_{E}, t_{T}, and r_{T} are indexed by the bed position b and the line of response (LOR), which itself is parametrized by s, the radial position, φ, the azimuthal angle, z, the mid-slice axial position, and Δ, the ring difference. In most cases, the indices will be hereafter omitted.

The global scale factors of the noiseless projections are arbitrary and the simulation does not predict the number of true, scattered, and random coincidences for the emission or transmission scan. For correct scaling, the total number of true ($N_{t\mathrm{E}}$, $N_{t\mathrm{T}}$), random ($N_{r\mathrm{E}}$, $N_{r\mathrm{E}}$), and scattered ($N_{s\mathrm{E}}$) coincident events have to be specified for some range $[b_1,b_2]$ of bed positions. Given these numbers, plus the half-life of the

[1]Address for Correspondence: SHFJ/DRM/DSV/CEA, 4 place General Leclerc, 91401 Orsay cedex, France. This work is supported by grants from the Swiss National Science Foundation, the Whitaker Foundation, and NIH grant CA74135. M.D. and C.M. are with the National Fund for Scientific Research (Belgium).

0-7803-5696-9/00/$10.00 (c) 2000 IEEE

isotope and the scan duration and the scan start time for each bed position, the noise level of the simulation will be defined by the global scale factors $\alpha_{t_E}(b)$, $\alpha_{r_E}(b)$, $\alpha_{s_E}(b)$, $\alpha_{t_T}(b)$ and $\alpha_{r_T}(b)$.

The simulation procedure is first to determine analytically the values of the noiseless sinogram elements and then to add pseudo-random Poisson noise, as described by (1) for individual sinogram elements

$$\begin{aligned} \tilde{p}_E &= P\left[\alpha_{t_E} \cdot t_E + \alpha_{r_E} \cdot r_E + \alpha_{s_E} \cdot s_E\right] \\ \tilde{p}_T &= P\left[\alpha_{t_T} \cdot t_T + \alpha_{r_T} \cdot r_T\right], \end{aligned} \tag{1}$$

where $\tilde{p}$ stands for the noisy "prompt" coincidences and $P[m]$ is a Poisson pseudo-random realization for the mean m. The corrected emission and transmission sinogram elements are calculated from the prompt coincidences by using procedures similar to what will be done in practice, with the difference that the same expectations $\alpha_{r_E} \cdot r_E$, $\alpha_{s_E} \cdot s_E$, and $\alpha_{r_T} \cdot r_T$ are used to generate the prompt coincidences and the correction terms. This is equivalent to assuming that the data correction procedures are completely accurate.

B. Emission and attenuation description

The value of the noiseless sinogram elements t_E, r_E, s_E, t_T and r_T are based on the specification of a geometry-based phantom, the geometry of the scanner, the position of the bed, and, for multi-bed acquisitions, the number of bed positions and the amount of bed overlap. In addition, measured blank sinograms $t_B(s, \varphi, z, \Delta)$ and normalization factors $\varepsilon(s, \varphi, z, \Delta)$ are also inputted to the simulation.

The geometry-based phantom is specified by a collection of 3D geometric shapes. Each shape consists in an ellipsoid object that can be cut by 2D planes with different orientations. Each object is characterized by its emission density $e(\mathbf{x})$ and its linear attenuation coefficient μ. We designed a whole-body phantom with a geometry based on the static MCAT phantom [3, 4], with the addition of a head, two arms, and a bladder (Figure 1).

The true coincidence elements t_E and t_T are determined by analytical projections along lines of response (LORs) through the emission and attenuation objects, and not by numerically projecting a voxelized image of the phantom. The effects of attenuation μ, normalization ε, and blank scan t_B are included in the determination of t_E or t_T

$$\begin{aligned} t_E &= \varepsilon^{-1} \cdot \frac{\sum_{\text{objects } i} \int_{\text{LOR}} e_i(\mathbf{x}) \mathrm{d}l}{\exp\left(\sum_{\text{objects } i} \int_{\text{LOR}} \mu_i \mathrm{d}l\right)} \\ t_T &= \varepsilon^{-1} \cdot \frac{\mathrm{Sm}\left[\varepsilon \cdot t_B\right]}{\exp\left(\sum_{\text{objects } i} \int_{\text{LOR}} \mu_i \mathrm{d}l\right)}, \end{aligned} \tag{2}$$

where $\mathrm{Sm}[\cdot]$ is a smoothing operator. Due to the potentially large area sampled by each detector pair, the value for the corresponding sinogram element is given by the average of a sub-sampled grid. The amount of oversampling is a user-specified parameter. To reflect the intrinsic spatial resolution of the scanner, the calculated projections are blurred by a 2D smoothing filter in the radial and axial directions.

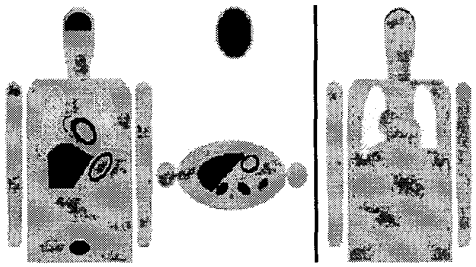

Figure 1: Coronal and transversal views of a whole-body geometry-based phantom. The following organs are visible in the emission phantom (left): brain, lungs, heart, stomach, kidneys, liver, spleen, spinal cord, and bladder. In the attenuation phantom (right), the skull and the ribs are visible.

C. Random and scattered coincidences

The exact calculation of r_E and s_E is computationally intensive. We therefore use an approximate model where the total activity in each slice is assumed to be concentrated along the axis of the scanner, and instead of the attenuating medium specified in the geometry-based phantom, we use a uniform cylinder of radius r and of linear attenuation coefficient μ_C. Furthermore, we assume that the sinogram elements for the scattered and random coincidences can be expressed as

$$\begin{aligned} r_E(s, \phi, z, \Delta) &= \varepsilon^{-1}(s, \phi, z, \Delta) \cdot r_E^{\perp}(s) \cdot r_E^{\shortparallel}(z, \Delta) \\ s_E(s, \phi, z, \Delta) &= \varepsilon^{-1}(s, \phi, z, \Delta) \cdot s_E^{\perp}(s) \cdot s_E^{\shortparallel}(z, \Delta) \\ r_T(s, \phi, z) &= \varepsilon^{-1}(s, \phi, z) \cdot r_T^{\perp}(s), \end{aligned} \tag{3}$$

and that the activity outside the FOV influences only the axial terms $r_E^{\shortparallel}(z, \Delta)$ and $s_E^{\shortparallel}(z, \Delta)$. This rough approximation is justified by the fact that the simulated data are then corrected for scattered and random coincidences assuming no bias, and only their influence on the noise is relevant.

The radial profiles $r_E^{\perp}(s)$, $s_E^{\perp}(s)$, and $r_T^{\perp}(s)$ are not calculated, but given as an input to the simulation. Typically, they are estimated by very high-count scans of a 20-cm diameter cylinder of uniform activity. The same radial profiles will be used regardless of the geometry of the simulated phantom.

Unlike the radial profiles, the axial profiles for $r_E^{\shortparallel}(z, \Delta)$ and $s_E^{\shortparallel}(z, \Delta)$ are calculated due to the greater dependance on source distribution. The axial profile of the random coincidences is given by the the single photon axial flux on the detector pair in coincidence. Only non-scattered photons are considered and, for acquisitions without septa, the single photon aperture for a given detector ring is limited by the shielding at both ends of the detector rings. If a 2D acquisition with septa in the FOV is simulated, we only consider single photons entirely contained within one slice.

To estimate the axial scatter profile $s_E^{\shortparallel}(z, \Delta)$, we assume that only one of the two emitted photons undergoes a single Compton interaction [5]. The calculation of the axial scatter profile is more complicated than for the random coincidences and involves three embedded integrations: one over the position of the positron annihilation along the scanner axis, one over the Compton scatter location in the attenuating medium μ_C, and one over the Compton scatter angle θ_C. For these reasons, we used a Monte Carlo integration technique based on the Klein-Nishina Compton scatter cross-section

formula to estimate the analytical axial profile of the scattered coincidences. As for the random coincidences, the positron annihilation occurs along the scanner axis and the attenuating medium μ_C where the Compton scatter takes place is contained within a uniform cylinder. The energy resolution and the lower energy threshold of the detectors are also included in the Monte Carlo integration. If a 2D acquisition with septa in the FOV is simulated, we again only consider Compton scatters entirely contained within one slice.

III. Simulation Validation Studies

To validate the expected noise properties of data simulated using the techniques described above, multiple acquisitions of groups of uniform cylinders were compared to multiple realizations of simulated data. A Siemens/CTI HR+ scanner was used to acquire data from 20-cm diameter and 20-cm length Ge-68/Ga-68 with different activity levels as described below. The use of Ge-68/Ga-68 allowed estimation of the variance across multiple acquisitions and to compare it with the variance estimated across several realizations of the simulation. The use of uniform cylinders simplified the replication and analysis of the measurements.

The ECAT HR+ scanner has 32 detector rings. The emission scans were performed without septa and a maximum detector ring difference of 22. LORs were mashed axially into five groups (called segments). The transmission scans were performed with septa and a maximum detector ring difference of 15.

A. Axial distribution for random and scattered coincidences

We first validated the models used to calculate the axial profiles $r''_{\mathrm{E}}(z,\Delta)$ and $s''_{\mathrm{E}}(z,\Delta)$ of the random and scattered coincidences for cylindrical phantoms. Measurements of the axial profiles were done with long duration emission scans of two cylinders with an activity ratio between the cylinders of 6.2 (43.91 MBq for the hot and 7.06 MBq for the warm cylinder). Three acquisitions were performed: one with only the warm cylinder within the FOV, one with the warm cylinder within the FOV and the hot cylinder just outside the FOV, and one with only the hot cylinder just outside the FOV and the warm cylinder removed. The random coincidences were stored separately (delayed coincidences) and the axial profile of the scattered coincidences was estimated using only the projections outside the cylinders, after correction for the random coincidences. Both acquired sinograms (prompt and delayed coincidences) were normalized with the same normalization factors.

To check that the predictions for the axial profiles are still plausible for whole-body phantoms, we inputted to the calculation of the axial profiles the pixel values of reconstructed images of real whole-body oncology scans. We selected three patients of increasing weight (54, 78, and 90 kg) and an anthropomorphic torso phantom, all scanned with FDG from the head to the bladder (Figure 2). Attenuation and scattered coincidences corrections were applied to the projections and the images were reconstructed with the OSEM algorithm [6]. The number of random coincidences was measured globally for each bed position and the scattered coincidences were estimated either with the routinely used procedure based on the *single scatter simulation technique* [7] or, for the anthropomorphic phantom, with the *estimation of trues method* (ETM) [8].

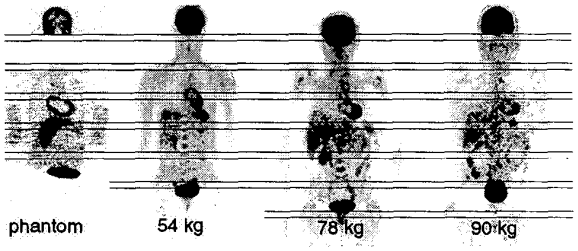

Figure 2: The four measured scans used to calculate the axial profiles of the random and scattered coincidences. The black horizontal lines correspond to the bed position limits with an overlap between adjacent bed position of 6.5 detector rings.

B. Fully corrected sinograms

Three cylinders of different activity (43.91, 7.06, and 2.00 MBq) were scanned over three bed positions with a 1 detector ring overlap between adjacent bed positions. For each bed position, 24 seperate 7-minute emission scans and 24 seperate 3-minute transmission scans were acquired. The total number of counts per acquisition for the first bed position (43.91 MBq cylinder) was typical of a clinical whole-body acquisition: 48M true, 52M scattered, and 47M random coincidences for the emission scan; 33M true and 3.6M random coincidences for the transmission scan. The total number of scattered coincidences was estimated with a fit procedure on the tails of the projection data outside the cylinder.

The measured data were corrected for random coincidences by on-line subtraction of the delayed coincidences. The attenuation correction factors ACFs were calculated as the ratio between the normalized and smoothed blank and transmission scans. The ACFs corresponding to non-null ring differences were calculated by forward-projecting the attenuation image reconstructed from the 2D ACFs. The scattered coincidences were corrected for by using the single scatter simulation technique implemented on the scanner [7].

All measured data were replicated with the whole-body simulator. The radial profiles $s^{\perp}_{\mathrm{E}}(s)$ and $r^{\perp}_{\mathrm{T}}(s)$ that should be given as an input to the simulation were estimated with a separate high-count acquisition of a 20-cm diameter cylinder. A uniform distribution was used for $r^{\perp}_{\mathrm{E}}$ as in practice the radial profile for random coincidences is very close to a uniform distribution. As only large objects, relative to the detector size, were simulated, we did not intend to replicate the spatial resolution of the scanner and hence the emission projections were not blurred.

The same data correction procedures as used for the measured data were applied to the simulated data, except for the scattered coincidences. The simulated corrected emission sinogram element was given by

$$\tilde{c}_{\mathrm{E}} = \widetilde{ACF} \cdot \varepsilon \cdot (\tilde{p}_{\mathrm{E}} - \mathrm{P}\left[\alpha_{r_{\mathrm{E}}} \cdot r_{\mathrm{E}}\right] - \alpha_{s_{\mathrm{E}}} \cdot s_{\mathrm{E}}) \qquad (4)$$

and the noisy $\widetilde{ACF}$ by

$$\frac{\alpha_{t_{\mathrm{T}}} \cdot \mathrm{Sm}\left[\varepsilon \cdot t_{\mathrm{B}}\right]}{\mathrm{Sm}\left[\varepsilon \cdot (\tilde{p}_{\mathrm{T}} - \mathrm{P}\left[\alpha_{r_{\mathrm{T}}} \cdot r_{\mathrm{T}}\right])\right]}. \qquad (5)$$

The noise level (parameters α) was given by the total number of coincidences in the first bed position acquisition.

IV. Results

A. Axial distribution for random and scattered coincidences

The comparison between the measured and the simulated axial profiles for random and scattered coincidences is shown in Figure 3 for 20-cm diameter cylinders. The scaling between the measured and the simulated data is based on the profile maximum for the first acquisition, with only the warm cylinder within the FOV. It should be noted that we had to include in the simulation the effect of the imperfectly shielded rod transmission sources by adding on the scanner axis a point source outside the FOV.

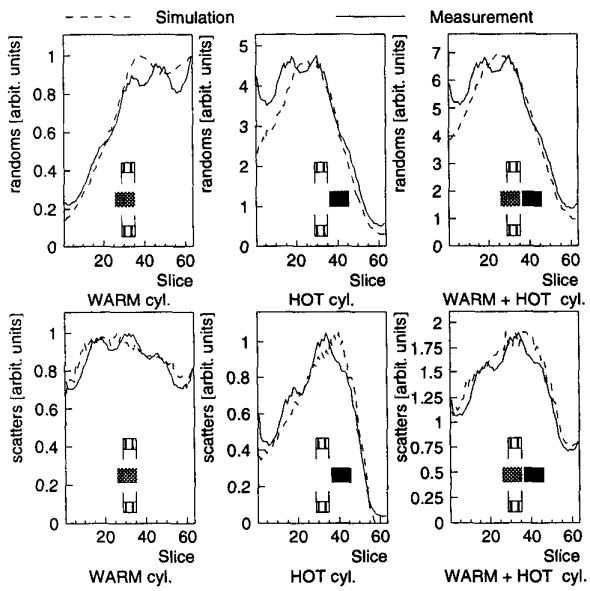

Figure 3: Comparison between the measured and the simulated axial profiles for random (top row) and scattered (bottom row) coincidences, for a ring difference Δ of zero.

In Figure 4, the axial profiles of the simulated scattered coincidences and the calculated scatter correction of the measured data are shown for each bed position acquisition of the anthropomorphic phantom. The scaling between the measured and the simulated data is based on the total number of scattered coincidences for the six bed positions together. It should be noted that, due to the geometry of the phantom, there is almost no activity within the second bed position. In Figure 5, the total number of random and scattered coincidences per bed position are shown for the three patients. It should be noted that for the 54 kg and the 90 kg patients, the head was scanned first, while the 78 kg patient was scanned in the opposite direction (from bed 8 to bed 1). The scaling between the measured and the simulated data is based on the total number of coincidences for all bed position, excluding the last bed position. In effect, the activity below the last bed position was not measured and hence its contribution to the random and scattered coincidences is ignored by the simulation.

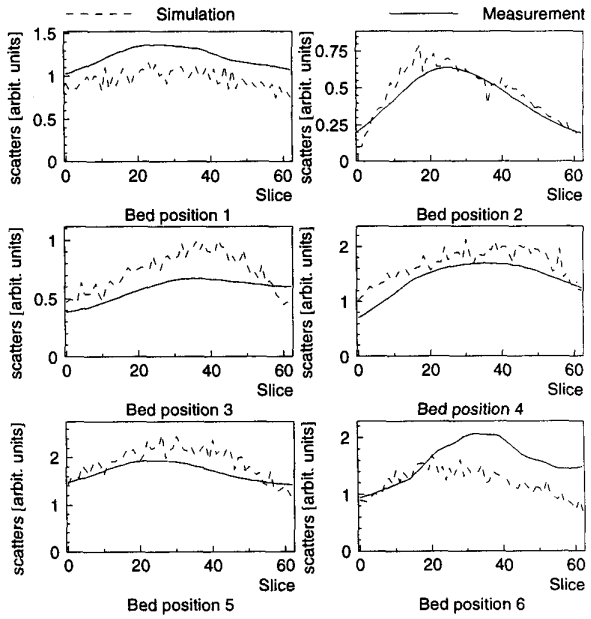

Figure 4: Comparison between the measured and the simulated axial profiles for scattered coincidences with the anthropomorphic phantom, for a ring difference Δ of zero.

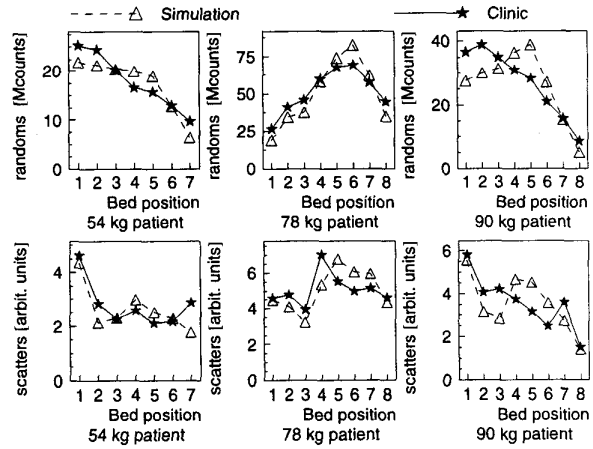

Figure 5: Total number of random (top) and scattered (bottom) coincidences per bed position for three patients.

B. Fully corrected sinograms

The standard deviation of the measured and simulated data was estimated across the 24 replications of each bed position acquisition. Figure 6 shows the absolute standard deviation at different steps of the data processing: raw emission data as they are acquired on the scanner (prompt minus delayed coincidences), attenuation correction factors (ACFs), and fully corrected emission sinograms. The standard deviation was averaged across the 144 azimuthal views φ. The first bed position corresponds to the slices 0 to 62, the second bed position to the slices 63 to 125, and the last bed position to the slices 126 to 188. The transition between the first (43.91 MBq)

and the second (7.06 MBq) cylinder occurs around slice 90 and the second cylinder ends around slice 185. It should be noted that there was an empty space between the cylinders of about 3 cm that was not included in the geometry-based phantom description (hence the differences for the ACFs between measured and simulated data in these empty spaces).

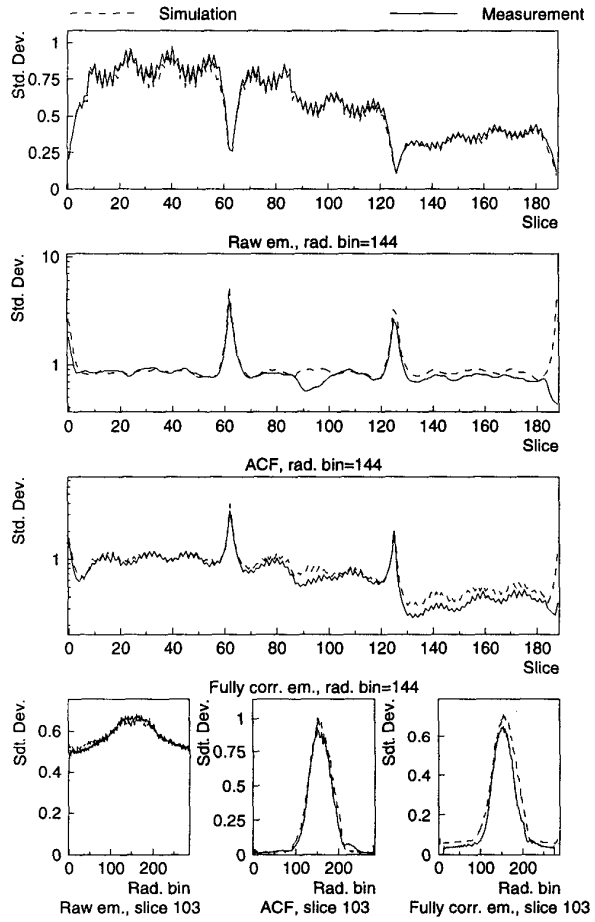

Figure 6: The absolute standard deviation of the measured and simulated data for the three bed positions acquisition and a ring difference of zero. The first three rows show the axial profiles and the last row the radial profiles.

V. Discussion

The simple model used to calculate the effect of the activity outside the FOV on the scattered and random coincidences consists of a centered non-uniform line source within a cold cylinder filled with water. Figure 3 shows the accuracy of the model for a cylindrical geometry and Figures 4 and 5 show that the model predicts plausible results for a more realistic whole-body geometry.

For the comparison with clinical data, in Figure 5, we observe several systematic effects. The simulation underestimates in the head and overestimates in the torso the number of scattered and random coincidences. This disagreement is related to the use of the same attenuating medium radius r for all bed positions. If more accuracy is wanted, the radius can be chosen different for the head and the torso. The simulation also underestimates in the last bed position the number of scattered and random coincidences. This effect is due to the fact that in the simulation, there is no activity after the last bed position.

The results of Figure 6 show that for an almost exact correspondence between the geometry-based phantom description and the physical phantoms used for the measurements, the agreement between the absolute standard deviation of the simulated and the measured data is very good. For the emission sinograms, both the measured and the simulated axial profiles exhibit patterns due to the normalization factors: the varying number of LORs contributing to each individual sinogram element and the detector block structure (four axial blocks per bed position corresponding to four bumps in the plots). It should be noted that the difference in the absolute standard deviation between the measured and the simulated fully corrected emission sinograms is related to the fact that the correction for scattered coincidences is accurate in the simulation while the correction technique used for the measured data is not exact, especially when there is a large amount of activity outside the FOV as in the third bed position.

VI. Conclusion

We have developed an analytical simulator of 3D whole-body PET scanning that takes into account the principle factors determinig the statistical noise and resolution properties of measured data. We showed that this whole-body simulator is able to predict realistic amounts of scattered and random coincidences as a function of the activity outside the FOV, and that the simulation of noisy transmission scans allows to replicate the noise introduced by the attenuation correction factors.

They are other features that are not simulated but can be incorporated in our simulator. These features include: dead-time (if we have an *a priori* model for the relationship between single photon rate and spatially varying dead-time), the emission contamination in post-injection transmission scans, and the scattered coincidences in the transmission scan.

VII. References

[1] S.S. Furuie *et al. Phys. Med. Biol.*, vol. 39, pp. 341–354, 1994.

[2] C. Comtat *et al. IEEE Trans. Nucl. Sci.*, vol. 45, no. 3, pp. 1083–1089, 1998.

[3] B.M.W. Tsui *et al. Investigative Radiology*, vol. 28, no. 12, pp. 1101–1112, 1993.

[4] K.J. LaCroix. PhD thesis, The University of North Carolina at Chapel Hill, Chapel Hill, NC, U.S.A., 1997.

[5] J.M. Ollinger *Phys. Med. Biol.*, vol. 41, pp. 153–176, 1996.

[6] H.M. Hudson and R.S. Larkin *IEEE Trans. Med. Imaging*, vol. 13, pp. 601–609, 1994.

[7] C.C. Watson *et al.* in *Proceedings of the 1995 International Meeting on Fully Three-Dimensional Image Reconstruction in Radiology and Nuclear Medicine*, pp. 255–268, Kluwer Academic, 1996.

[8] B. Bendriem *et al.* in *Conference Record of the 1993 IEEE Nuclear Science Symposium and Medical Imaging Conference*, vol. 3, pp. 1779–1783, 1993.